Conformation of a Rigid Tetrasaccharide Epitope in the Capsular Polysaccharide of *Vibrio cholerae* O139[†]

Shamantha Gunawardena,[‡] Cara R. Fiore,[§] Judith A. Johnson,[§] and C. Allen Bush*,[‡]

Department of Chemistry & Biochemistry, University of Maryland Baltimore County, Baltimore, Maryland 21250, and Departments of Pathology and Medicine, University of Maryland School of Medicine and Veterans Affairs Maryland Health Care System, Baltimore, Maryland 21202

Received May 5, 1999; Revised Manuscript Received June 18, 1999

ABSTRACT: A newly reported strain of *Vibrio cholerae*, known as strain O139 Bengal, is the first instance of an encapsulated strain that has caused epidemic cholera. The O-antigenic capsule is the critical antigen for protective immunity. Since mapping of the antigenic epitopes will assist in the development of a protein conjugate vaccine based on the capsular polysaccharide, we have undertaken a study of the three-dimensional conformation of the polysaccharide. It contains six residues in the repeating subunit with the unusual feature of a 4,6 cyclic phosphate on a β-galactopyranoside. A structural epitope composed of four of the residues is somewhat similar to the Lewis^b blood group tetrasaccharide. Polysaccharide samples enriched in ^{13}C have been prepared by growth of the bacteria in ^{13}C-enriched medium. Multidimensional heteronuclear NMR and molecular modeling studies are reported, which show that the O139 tetrasaccharide adopts a compact and tightly folded conformation that is relatively rigid and similar to the Le^b conformation. The cyclic phosphate on the β-galactopyranoside residue is in contact with the colitose residue linked to the β-GlcNAc.

All the cholera epidemics known in recent times have been caused by *Vibrio cholerae* of the serotype O1 carrying the cholera toxin (CT)[1] genes. The O1 designation refers to the LPS O-polysaccharide chain, which is known to be a homopolymer of the somewhat unusual sugar 4,6-dideoxy-4-aminomannose (perosamine). But in 1992, a new epidemic type of cholera was discovered that is caused by *V. cholerae* that are not cross-reactive with O1 strains and are designated as O139 (*1*). This development has stimulated considerable interest in various aspects of *V. cholerae* O139 strains, which, unlike the O1 strains, have a capsular polysaccharide (*2*−*4*). O139 strains are in most ways similar to O1 strains in that they carry CT genes, but they differ in the synthesis of the LPS and capsule (*5*). Since patients in regions of the world where cholera is endemic have immunity to O1 strains but not to the O139 strains, the latter have spread rapidly, supplanting O1 strains as the major epidemic strains in some regions of India (*6*).

We have previously reported on the chemical structure of the capsular polysaccharide from *V. cholerae* O139. Using primarily NMR data, we proposed a structure containing six sugar residues in the repeating subunit, which includes the unusual feature of a cyclic phosphate on a galactopyranosyl residue (*7*). Subsequently, methylation analysis and other chemical techniques have confirmed the proposed structure, shown in Figure 1, including the unusual feature of the cyclic phosphate (*8*). Serological cross-reaction has been noted between the capsule and the lipopolysaccharide (LPS) from the *V. cholerae* O139 (*2*) and it has been shown that the LPS has an O-polysaccharide chain that terminates in a single hexasaccharide whose structure is identical to that of the repeating subunit found in the capsule, including the 4,6 cyclic phosphate (*9*).

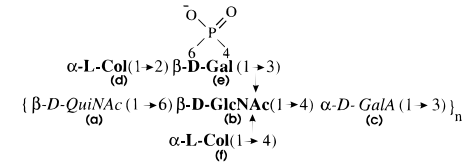

FIGURE 1: Schematic representation of capsular polysaccharide structure of *V. cholerae* O139. Tetrasaccharide epitope homologous to Le^b histo-blood group antigen is shown in boldface type. Labeling **a**-**f** is according to Preston et al. (*7*).

The capsular polysaccharide has been proposed as the basis for vaccine development (*10*). Information on the three-dimensional conformation of this polysaccharide will be helpful as a basis for mapping of the various epitopes of this complex polysaccharide to determine which are antigenic and protective. In the present study, we show by NMR and molecular modeling methods that four sugar residues in this hexasaccharide form a very compact tetrasaccharide epitope with a relatively rigid conformation.

[†] This research was supported by NSF Grant MCB 97-24133 and by NIH Grants AI-28856 and GM-57211.

* Corresponding author: Phone (410) 455-2506; fax (410) 455−2608; e-mail bush@umbc.edu.

[‡] Department of Chemistry & Biochemistry.

[§] Departments of Medicine and Pathology

[1] Abbreviations: NOESY, nuclear Overhauser effect spectroscopy; HMQC, heteronuclear multiple quantum coherence; DQF COSY, double quantum filtered coherence spectroscopy; CT, cholera toxin; LPS, lipopolysaccharide; FID, free induction decay; ELISA, enzyme-linked immunosorbent assay; CPS, capsular polysaccharides.

10.1021/bi9910272 CCC: $18.00
Published on Web 08/21/1999

MATERIALS AND METHODS

Samples of the capsular polysaccharide were isolated from *V. cholerae* strain AI1837, which has been well-characterized and has been shown to cause cholera in healthy North American volunteers (*11*). Single bacterial colonies grown from frozen glycerol stocks were inoculated into L-broth for 18 h of growth at 30 °C. One milliliter of each culture was spread on 1 L of solid medium in 8−10 150 mm Petri dishes and incubated for 48 h at 37 °C. Capsular polysaccharide was isolated as previously described (*12*). Natural abundance samples were grown on L-agar (1% bacto-tryptone, 0.5% yeast extract, and 1% NaCl).

Prior to use of labeled glucose for the purpose of obtaining ^{13}C-labeled polysaccharides, a series of growth curves was analyzed to determine the optimum culture conditions and to explore the possibility of substitution of an algal hydrolysate (Celtone, Martek Inc., Columbia, MD) for the tryptone to facilitate stable isotope incorporation. For this purpose, 100 mL of liquid medium was inoculated and shaken at 37 °C. Growth of bacteria was monitored hourly, from the change in turbidity measured as optical density at 600 nm. Varying amounts of Celtone, tryptone, and glucose, in M-9 minimal medium, were studied. Efficient growth was found with 1% tryptone or 0.2% Celtone supplemented with 0.02−0.2% glucose in M-9 minimal medium.

For the preparation of selectively ^{13}C-labeled capsular polysaccharide, cultures were grown on M9 minimal medium supplemented with 0.8% bacto-tryptone (Difco, Detroit, MI) and 0.1% filter-sterilized [*1*-^{13}C]glucose. Medium was solidified with 15 g/L ultrapure agarose (Gibco−BRL, Grand Island, NY). The uniformly ^{13}C-enriched polysaccharide was grown on M9 medium supplemented with 0.2% NaCl, 0.2% filter-sterilized [*u*-^{13}C]Celtone-C and 0.1% fermentation-grade [*u*-^{13}C]glucose (Martek). Polysaccharide was isolated as described above, extensively sonicated in ice, and then purified by size-exclusion chromatography on a Bio-Gel P6 column (2 × 100 cm) with water as the eluent. Fractions eluting at the void volume were lyophilized and used for NMR experiments.

Polysaccharide samples were exchanged three times with D_2O and made up in high-purity D_2O in 5 mm NMR tubes at a concentration of approximately 8 mg/mL. Natural-abundance samples were studied at 500 MHz ^{1}H frequency on a GE Omega PSG spectrometer at a probe temperature of 60 °C. Two-dimensional NOESY spectra were recorded at mixing times from 40 to 200 ms with standard pulse sequences. Selective T_1 were measured with selective inversion pulses (180°) of 40 ms in length with the carrier centered on each of two isolated anomeric resonances at 5.407 and 5.035 ppm. Data were processed on a Silicon Graphics Indigo workstation with the Felix software (Biosym Corp.).

All spectra of the uniformly highly ^{13}C-labeled O139 polysaccharide were recorded on a GE Omega PSG instrument, operating at 600 MHz. HMQC spectra with and without ^{13}C decoupling were acquired with the ^{13}C carrier set at 81.6 ppm with a ω_1 spectral width of 10931 Hz, thus folding methyl carbons between anomeric and ring resonances and 3-deoxy carbons downfield of anomeric resonances in the ^{13}C dimension. This made it possible to prevent overlap of these methyl resonances with signals of anomeric and ring resonances in any given ω_2 vector. The final matrix sizes of the 2D HMQC spectra of the uniformly ^{13}C-labeled sample was 1K × 1K. The spectra were processed with addition of 32 points to each FID in the ^{13}C dimension with linear prediction, prior to apodization. To measure $^1J_{CH}$ from ^{13}C-coupled HMQC, the vector containing the two cross-peak components in, ω_2 was reverse Fourier-transformed and the new FID was zero-filled and transformed to achieve a 1D spectrum with a resolution of 0.2 Hz, from which the couplings were measured by estimating the separation between the two components.

Three-dimensional HMQC-NOESY (*13*) with 32, 64, and 256 complex points in, t_1, t_2, and t_3, respectively, were recorded with mixing times of 40 and 100 ms. Proton (ω_2 and ω_3) and carbon (ω_1) dimensions were set according to HMQC parameters described above, so that NOE from the diagonals whose attached ^{13}C resonance were folded in ω_1 would not share the same ω_3 vectors of unfolded anomeric or ring resonances. ^{13}C decoupling in t_2 was achieved with a composite proton 180° in the middle of evolution and by applying GARP decoupling in acquisition dimension t_3. Selective proton T_1 was measured for the isolated satellites of **c** H1 and the downfield satellite of **d** H1.

The final matrix of the 3D HMQC-NOESY generated for uniformly enriched O139 sample was 512 × 512 × 1024 (ω_1, ω_2, and ω_3 respectively) in real data. The first points of FIDs in the ^{13}C dimension were calculated by linear prediction and the FIDs along the ^{13}C and ^{1}H evolution dimensions were extended by 24 and 32 points by linear prediction. NOESY cross peaks for any pair of protons can be found on two different ^{13}C planes. Experimental NOE intensity was calculated as the average intensity of these two components if they were well isolated; otherwise only one component was considered. Because we could measure selective T_1 for both satellites only for **c** H1, each NOESY cross-peak was normalized with respect to its diagonal peak intensity.

Molecular modeling was done with the CHARMm software with either Quanta or Insight for graphical manipulations of the models (both from MSI Corp., San Diego, CA). Potential energy functions of CHARMm were used as modified for carbohydrates (*14*). All calculations were done in a vacuum without explicit inclusion of water with a distance-dependent dielectric constant and a cutoff at 15 Å. The glycosidic dihedral angles Φ and Ψ, are defined according to the IUPAC convention by $O_5-C_1-O-C'_x$ and $C_1-O-C'_x-C'_{x-1}$. Relaxed conformational energy maps were constructed for each of the three disaccharides, **d-e**, **e-b**, and **f-b**, by constrained energy minimization as a function of Φ and Ψ dihedral angles with a 10° step size. (See Figure 1 for labeling of the residues.) All the low-energy disaccharide conformations were combined to form tetrasaccharides. These tetrasaccharides were energy-minimized to relax all dihedral angles, and these low-energy tetrasaccharide models were selected for conformational analysis by use of NOE data.

NOESY spectra were simulated from conformational models by the matrix method (*15*). Experimental cross-peak volumes were scaled by using the selective T_1 data to represent a fraction of V_0, the volume of a diagonal peak at zero mixing time (*16*, *17*). To account for heteronuclear dipolar relaxation in the NOESY simulations for the uniformly ^{13}C-enriched polysaccharide, the contribution of

Table 1: Heteronuclear One-Bond ($^1J_{CH}$) Couplings of O139 CPS[a]

coupled nuclei	residue					
	β-QuiNAc **a**	β-GlcNAc **b**	α-GalA **c**	α-Col **d**	β-Gal(P) **e**	α-Col **f**
C1−H1	161.7	162.3	175.5	174.0	159.4	170.5
C2−H2	136.2	135.9	*b*	142.0	141.3	142.0
C3−H3	141.4	138.0	138.8	123.0	138.2	123.0
C3−H3′				123.0		123.0
C4−H4	142.7	142.7	150.8	149.6	150.2	149.6
C5−H5	137.7	134.6	143.3	142.7	138.9	142.9
C6−H6	123.6	160.6		123.6	158.0	123.6
C6−H6′		157.8			164.0	
$C_{Me}-H_{Me}$[c]	125.5	125.5				

[a] Coupling constants (in hertz) were measured by HMQC without ^{13}C decoupling during acquisition; experimental error is ±0.4 Hz. [b] Overlapped peaks from which couplings cannot be measured accurately. [c] In *N*-acetyl group.

attached ^{13}C nuclei on proton relaxation, an autorelaxation term by the attached ^{13}C, is included (*18*). A single tumbling correlation time for the tetrasaccharide was estimated by fitting intraresidue theoretical and experimentally observed NOEs. Agreement between experimental and theoretical data were evaluated by calculating agreement factors proposed by Shriver and Edmondson (*19*):

$$R = \frac{\sum|\mathrm{NOE_o} - \mathrm{NOE_c}|}{\sum|\mathrm{NOE_o}|}$$

$$R_\mathrm{d} = \frac{\sum||\mathrm{NOE_o}|^{1/6} - |\mathrm{NOE_c}|^{1/6}|}{\sum|\mathrm{NOE_o}|^{1/6}}$$

where NOE_o and NOE_c refer to the experimentally observed intensities and calculated NOE intensities from model structures, respectively.

RESULTS

Although determination of the puckering of the pyranoside sugar residues is generally straightforward, the structure of Figure 1 has two unusual features that deserve attention. First is the α-colitose residues, which have two bulky axial substituents in both the $^1C_4$ and the $^4C_1$ conformation. Two lines of evidence indicate that both residues adopt the normal $^1C_4$ puckering common for L sugars. First, DQF COSY spectra (data not shown) show much larger cross-peaks between H2 and the axial H3 for the two colitose residues **d** and **f** than between H3 and H4 of those residues, indicating that H2 is axial and H4 is equatorial for both residues. Second, $^1J_{CH}$ values that are smaller (<145 Hz) for axial protons than for equatorial protons (>145 Hz) (*20*) indicate (Table 1) that the colitose residues **f** and **d** are in the $^1C_4$ chair form, which is normal for sugars in the L-galacto configuration. The stereochemistry of abequose, the D-isomer of colitose, found in the repeating unit of *Salmonella* serogroup B O-polysaccharide, has been extensively studied by Bundle et al. (*21*), whose X-ray crystallographic studies have shown that the D-isomer of 3,6-dideoxygalactose forms a $^4C_1$ chair.

A second problem requiring attention is the conformation of the bicyclic ring of the 4,6 cyclic phosphate β-galactose, a structure that has not previously been modeled in carbohydrates. Both homonuclear coupling constants $^3J_{HH}$ (not shown) and the heteronuclear one-bond $^1J_{CH}$ data (Table 1) indicate a normal $^4C_1$ chair conformation for the galactose residue, **e**. A chair conformation can be conveniently built for the cyclic phosphate ring in which the ^{31}P is trans to one of the H6 protons of Gal and gauche to the other H6 as well as to H4. Hall and Malcolm (*22*) have reported $^3J_{PH}$ values for a model cyclic phosphate in a chair conformation. The measured $^3J_{PH}$ for the O139 polysaccharide (not shown) as well as the data reported by Knirel et al. (*8*) for an oligosaccharide fragment from the polysaccharide are consistent with such a chair conformation. These observations are also consistent with the stereospecific assignment of the H6 of Gal that can be made with 3D HMQC-NOESY data as will be discussed below.

Given the conformations of the pyranoside rings of the sugars, molecular modeling of the tetrasaccharide is possible. Following the procedures in Materials and Methods, several different low-energy disaccharide conformational models for the three disaccharides were identified within 7 kcal/mol. Six distinct minima were found for both **e-f** and **f-b** disaccharides, and three low-energy conformations were exhibited by disaccharide **d-e** (Table 2). Although the disaccharide models all showed normal chair conformations for residues, **b**, **d**, and **f**, several instances of distorted chair conformations were observed for residue **e**. These conformers, not consistent with the experimental coupling data discussed above, were not further considered.

Tetrasaccharide models including the residues **d-e-b-f** (Figure 1) were built for the 108 combinations of minimum energy disaccharide conformations discussed above. They were energy-minimized with respect to all degrees of freedom, using steepest descent and conjugate gradient algorithms. Resultant minima showing any chair distortions described above were discarded. The resulting tetrasaccharide conformations were grouped into families with glycosidic torsion angles Φ and Ψ differing by less than 15°. Thirteen distinct tetrasaccharide conformational families were identified and the lowest energy conformer of each is listed in Table 3. Thus M1, the global minimum, belongs to family I, and M2−M13 are the minimum energy conformations of the rest of the families, which lie within 10 kcal/mol of the global minimum. While the energies associated with tetrasaccharide conformations are not absolutely accurate, we believe the sampling procedure locates all the important low-energy conformations.

The 2D NOESY spectra of the natural abundance polysaccharide recorded at mixing times of 40, 80, 120, and 200 ms showed that negative NOEs develop very rapidly in this system. NOE intensities were normalized with respect to diagonal peak intensities of the two isolated anomeric signals at zero mixing time (described in Materials and Methods) using selective proton T_1 of **c** H1 (277.3 ms) and **d** H1 (287.3 ms). The effective rotational correlation time τ_c was treated as an adjustable parameter to give the best fit of simulated intraring NOE values with the experimental data on model M1. This value, 5.7 ns, is an estimate of the approximate effective correlation time, since the calculated intraring NOE cross-peak intensities depend mainly on τ_c rather than on the details of the conformational model.

NOESY at a mixing time of 40 ms, shown in Figure 2, indicates a number of strong intraresidue cross-peaks as well

Table 2: Low-Energy Conformations from Disaccharide Modeling

disaccharide	minima	dihedral angles (deg) Φ^a	dihedral angles (deg) Ψ^b	relative energy (kcal/mol)
Col-α(1 → 2)-β-D-Gal4,6(PO_4) [**d-e**]	1	−51.6	158	0
	2	−113.0	114.0	1.0
	3	−64.7	−43.1	2.1
D-Gal4,6(PO_4)-β(1 → 3)-β-D-GlcNAc [**e-b**]	1	16.7	53.2	0
	2	26.3	54.8	1.1
	3	−64.4	−137.0	4.0
	4	41.8	72.1	4.3
	5	−99.4	−141.0	6.1
	6	−106.0	58.6	6.9
Col-α(1 → 4)-β-D-GlcNAc [**f-b**]	1	−109.0	−67.5	0
	2	178.0	58.6	0.7
	3	−178.0	55.2	0.9
	4	−86.4	54.6	2.6
	5	−60.5	−29.9	2.9
	6	18.8	143	3.3

[a] $\Phi = O_5-C_1-O-C'_x$. [b] $\Psi = C_1-O-C'_x-C'_{x-1}$.

Table 3: Tetrasaccharide Conformational Families Derived from Relaxed Energy Mapping Procedure[a]

	glycosidic dihedral angles[c]						
	Col-α(1 → 2)Gal4,6(P)		Gal4,6(P)-β(1 → 3)GlcNAc		Col-α(1 → 4)GlcNAc		relative[d] energy (kcal/mol)
minima[b]	Φ_1	Ψ_1	Φ_2	Ψ_2	Φ_3	Ψ_3	
M1	−98.7	125.0	−66.3	−103.0	−56.7	143.0	0
	(−99.3 −98.7)[d]	(124 125)	(−66.3 −65.3)	(−104 −103)	(−56.7 −55.6)	(143 144)	
M2	−114.0	114.0	−57.7	−103.0	−138.0	72.5	3.3
	(−115 −110)	(114 120)	(−60.7 −57.7)	(−105 −102)	(−141 −138)	(72.5 75.9)	
M3	−92.1	118.0	−3.7	68.2	−38.2	172.0	5.1
	(−96.1 −92.1)	(115 119)	(−4.9 3.5)	(65.9 70.2)	(−38.2 −35.9)	(172 175)	
M4	−113.0	112.0	−60.5	−90.2	−59.5	−34.0	5.5
	(−113 −112)	(112 113)	(−61.7 −60.5)	(−90.4 −90.2)		(−34.3 −34)	
M5	−93.6	117.0	8.2	59.6	−102.0	−74.1	5.8
	(−93.6 −81)	(109 117)	(8.2 27.1)	(57 59.6)	(−105 −102)	(−74.1 −72.1)	
M6	−99.4	142.0	−60.4	65.5	−62.4	−41.4	6.1
M7	−95.5	141.0	−65.0	−62.3	−156.0	−91.7	6.6
M8	−92.0	111.0	21.8	61.3	−89.6	47.6	7.6
	(−97.9 −88.8)	(111 120)	(21.8 23.8)	(61.3 62.5)	(−99.6 −88.5)	(47.6 65.3)	
M9	−97.8	117.0	25.0	62.0	−61.5	−33.0	8.8
	(−104 −93.6)	(112 120)	(24.4 36.9)	(59.8 85)	(−80.6 −60.7)	(−40.1 −32.7)	
M10	−104.0	128.0	−79.2	−91.9	−95.6	−83.0	8.9
	(−104 −103)	(128 −131)	(−82.9 −79.2)	(−94.5 −91.9)	(−95.6 −95.2)	(−83 −82.8)	
M11	−105.0	132.0	−58.1	72.5	−71.2	19.8	9.5
M12	−102.0	124.0	28.4	67.8	−39.0	−173.0	9.7
	(−102 −101)		(28.4 35.1)	(67.8 70.7)	(−42.6 −39)	(−173 −169)	
M13	−101.0	120.0	39.3	78.9	−97.1	−73.8	10.1
			(38.9 39.3)			(−74 −73.8)	
Le[b] [e]	−75.0	138.0	−61.0	−111.0	−62.0	148.0	

[a] Families are characterized by their conformation of lowest energy and the possible range in glycosidic torsion angles. Only families whose local minimum is within 10 kcal/mol from the global minimum are listed. [b] Represents the lowest energy conformational model of each family. [c] "Heavy atom convention" has been used to define dihedral angles of conformational minima. [d] Range of dihedral angles (i.e., the minimum and the maximum torsion angle of the cluster of conformations) for each family is indicated in parentheses, under the dihedral angle of its minimum energy model. If range is not indicated, it could be either because the entire cluster shows similar dihedral angles or because only one conformational model was found in that family. [e] Torsion angles according to ref *33*.

as interresidue peaks including peaks across linkages and some long-range correlations. Large cross-peaks are observed between the anomeric protons to aglycon protons for Col[2] **d** H1 to Gal **e** H2, for Gal H1 to GlcNAc **b** H3, and for Col[4] **f** H1 to GlcNAc H4. A large peak is also seen for GlcNAc H1 to GalA **c** H4 and somewhat weaker peaks appear between GalA H1 and QuiNAc **a** H3 and between QuiNAc H1 and GlcNAc H6. There are strong cross-peaks between protons on residues that are not directly connected, such as Col[2] **d** H5 and GlcNAc H2. There is also a strong cross peak between Col[4] **f** H1 and GlcNAc H6. The long-range connectivities, in particular the ones between H5 of colitose **f** and H2 of galactose **e** and between H5 of colitose **d** and H2 of glcNAc **b**, suggest a folded conformation for the tetrasaccharide composed of residues **b**, **d**, **e**, and **f**. However, only a very few cross-peak intensities can be accurately measured, especially in the ring region, because of overlaps, making it harder to use these data for an accurate conformational analysis.

Due to these overlaps, biosynthetic enrichment in ^{13}C was explored as a method for improving resolution for the NOESY spectra through ^{13}C editing. When glucose ^{13}C-labeled at the C1 position was used together with unlabeled tryptone (culture procedure described in Materials and

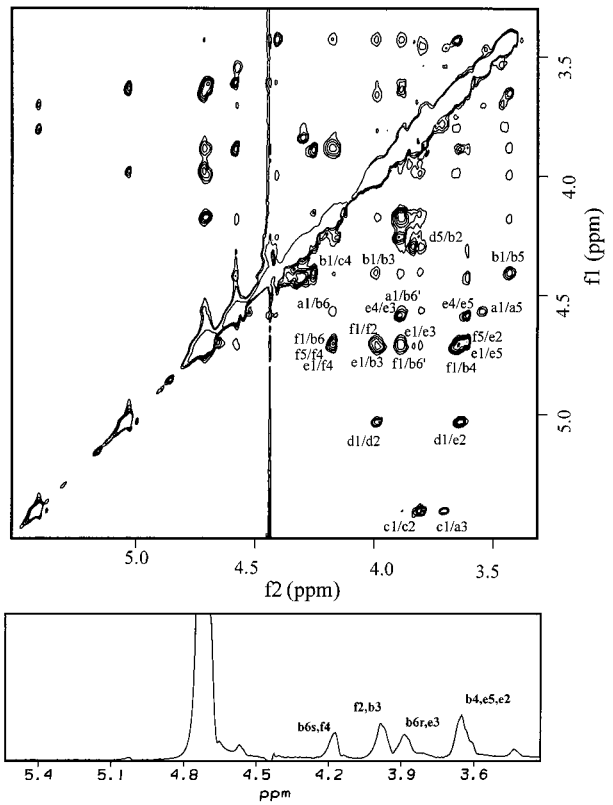

FIGURE 2: NOESY spectrum (500 MHz) of the natural-abundance capsular polysaccharide of *V. cholerae* O139 at 60 °C and a mixing time of 40 ms with row at 4.7 ppm containing resonances of **f1**, **e1**, and **f5**. For simplicity, the **c**H1/**c**H2 cross-peak is labeled as c1/c2, etc.

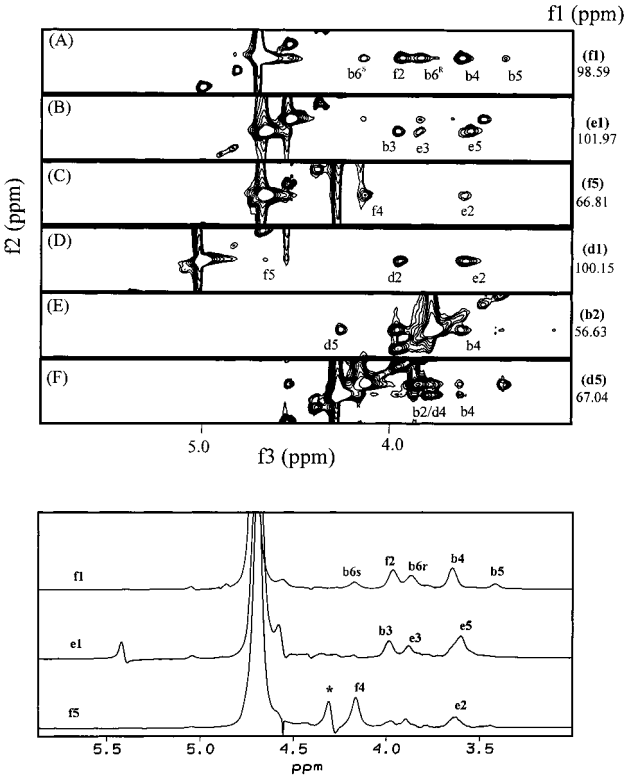

FIGURE 3: Two-dimensional NOESY strips ($\omega_2-\omega_3$) and 1D projection from 600 MHz 3D HMQC-NOESY (at 40 ms mixing time) across selected ^{13}C planes (ω_1) (as indicated on the right-hand side) with interresidue NOE connectivities. Panel A shows NOESY cross-peaks between **f** H1 (donor) and its recipients on **f** C1 plane at 98.59 ppm. For simplicity only the recipients are labeled; thus **b5** on strip A indicates the **f**H1/**b**H5 ($\omega_2-\omega_3$) cross-peak, etc.

Methods), capsular polysaccharides primarily ^{13}C-labeled at the anomeric and methyl carbon atoms were produced. For polysaccharide samples grown in 0.1% [1-^{13}C]glucose, 1D ^{1}H spectra (not shown) show the integral intensity of ^{13}C satellites of the downfield anomeric ^{1}H signals to have 70% of the total intensity. The satellites of *N*-acetyl methyl resonances of QuiNAc and GlcNAc show 40% of their total proton resonance intensity (data not shown), indicating 70% and 40% ^{13}C enrichment at these sites, respectively. Twenty-five percent of 6-deoxy methyl carbons of quiNAc and the two colitose residues are ^{13}C-enriched. Since satellites could not be observed for ring resonances between 3.4 and 4.7 ppm, ^{13}C enrichment for these resonances was determined from ratios of their HMQC cross-peak intensities to those of HMQC intensities of anomeric signals whose ^{13}C enrichment levels were determined from the 1D ^{1}H spectra. Necessary corrections for differences in HMQC intensities resulting from differential relaxation effects and differences in $^1J_{CH}$ values were made with the natural-abundance HMQC spectrum. This procedure indicated that the ring carbon atoms, including the 3-deoxy sites of colitoses, were not significantly enriched above natural abundance.

These results are consistent with direct incorporation of C1-labeled glucose with a small proportion being catabolized prior to incorporation as observed by Jones and Sanders (*23*) for the *Klebsiella* K3 serotype capsular polysaccharide. Similar studies on alginate biosynthesis in *Azotobacter vinelandii* (*24*) did not show transfer of ^{13}C1 into C6 of sugar residues, implying no scrambling of ^{13}C isotope from C1 to other carbon atoms via triose pools. Such direct incorporation of singly ^{13}C-labeled glucose allowed Sheng and Cherniak (*25*) to randomly enrich different carbons biosynthetically in the glucuronoxylomannan of *Cryptococcus neoformans* using a cocktail of ^{13}C-labeled sugars each enriched at a different carbon site. Biosynthetic ^{13}C enrichment of *Escherichia coli* O25 O-polysaccharide (*26*) also showed direct incorporation of ^{13}C-labeled glucose.

When uniformly ^{13}C-enriched glucose was used in the culture medium together with ^{13}C-labeled Celtone as the source of amino acids in the bacterial culture medium, the resulting polysaccharide was uniformly highly enriched in ^{13}C, similar to our observations with the cell wall polysaccharide from *Streptococcus mitis* J22 (*27*). One-dimensional proton spectra of the fully ^{13}C-enriched O139 polysaccharide sample show that all signals are split into their ^{13}C satellites with small central peaks from ^{12}C (data not shown) indicating 95% enrichment. The intensities of all HMQC peaks for this sample are identical to those of the natural-abundance sample, indicating 95% uniform ^{13}C enrichment.

Due to the good chemical shift dispersion in the ^{13}C dimension as seen in an HMQC (*7*), a substantial improvement in the resolution of the NOESY spectrum is observed in the ^{13}C-edited 3D HMQC-NOESY spectrum. NOESY strips in Figure 3 demonstrate how peak overlap in 2D NOESY has been effectively overcome by 3D ^{13}C-edited NOESY. As shown in Figure 2, cross-peaks **f** H5/**e** H2, **e** H1/**e** H5, and **f** H1/**b** H4 are severely overlapped in 2D NOESY of natural-abundance O139 polysaccharide because

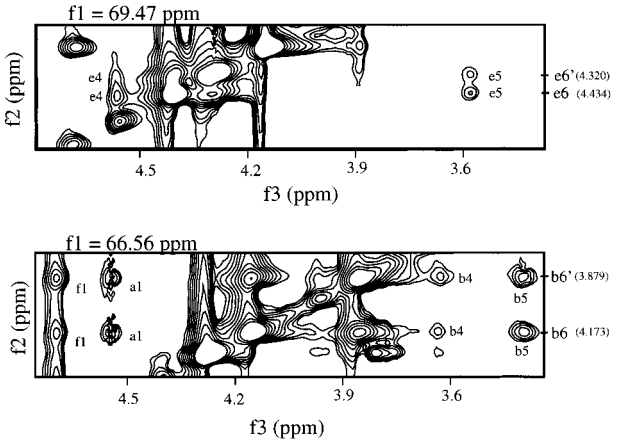

FIGURE 4: Two-dimensional NOESY strips from 600 MHz 3D HMQC-NOESY at 40 ms mixing time, across **e** C6 and **b** C6 ω_1 planes, showing NOE cross-peaks of H6 with intraresidue H4 and H5. Stereospecific assignments were made by using the intensities of these peaks.

proton chemical shifts of both the donors (**f** H5, **e** H1, and **f** H1) as well as their recipients (**e** H2, **e** H5, and **b** H4) show degeneracy, complicating accurate NOE quantitation. However, ^{13}C shifts of these two sets of resonances show excellent dispersion, making it possible to separate these overlapped cross-peaks as shown in Figure 3.

Resolved NOE peaks from H4 to H6 and H6′, as well as from H5 to H6 and H6′, enable stereospecific assignment and determination of the orientation of exocyclic hydroxymethyl groups of residues **b** and **e**. In the bicyclic galactophosphate (residue **e**), the cyclic phosphate moiety assumes a chair conformation restricting O6, H6, and H6′ of galactose (**e**) to a *gg* conformation. The NOE cross-peak between **e** H5 and **e** H6 is similar in intensity to that between **e** H5 and **e** H6′, while the NOE between **e** H4 and **e** H6 is stronger than that between **e** H4 and **e** H6′ (Figure 4). This implies that the downfield **e** H6 is *pro-R* (**e** H6^R) and that the upfield **e** H6′ is *pro-S* (**e** H6^S). In residue **b** (GlcNAc), the NOEs between **b** H5 and **b** H6 and between **b** H5 and **b** H6′ are similar, while **b** H4/**b** H6 is weaker than **b** H4/**b** H6′, indicating that the downfield **b** H6 is *pro-S* (**b** H6^S) and the upfield **b** H6′ is *pro-R* (**b** H6^R).

NOE cross-peak intensities from 3D HMQC-NOESY of the uniformly highly enriched O139 sample were normalized the same way as natural abundance NOEs (i.e., experimental NOE intensities divided by V_0). Selective T_1 values were shorter than natural-abundance T_1 values as expected. Moreover, the downfield satellite of **c** H1 showed a shorter selective T_1 (123 ms) than the upfield satellite (181 ms), implying that at higher mixing times the upfield satellite contributes more to the ^{13}C-decoupled NOESY intensities. Therefore, for NOE at 100 ms mixing time, intensities were normalized with respect to V_0 of the **c** H1 diagonal peak calculated from the selective T_1 of its upfield satellite, while at a shorter mixing time of 40 ms, the average of V_0 derived separately from the selective T_1 values of the two satellites of **c** H1 was used to normalize cross-peak intensities. The same effective rotational correlation time (5.7 ns) as for the natural-abundance sample was determined by fitting intraresidue experimental and calculated NOE intensities from all residues. Using this τ_c, we have simulated NOESY intensities of all experimentally observed interresidue NOE peaks at 40 ms mixing time for all the conformational minima M1−M5 having energies within 6 kcal from the global minimum (Table 4). Similar calculations were carried out with the same rotational correlation time at a NOESY mixing time of 100 ms (not shown). R_d, which is calculated as the inverse sixth power of NOE intensities (shown in Materials and Methods), was chosen for evaluation of the agreement of simulated intensities with experimental NOE values because it reflects more accurately the differences in distances (*19*).

Table 4: Experimental[a] and Simulated NOESY Intensities[b] for d-e-b-f Tetrasaccharide[c] of ^{13}C-Enriched Polysaccharide

		NOE$_{calc}$[f]				
cross-peak[d]	NOE$_{expt}$[e]	M1	M2	M3	M4	M5
e1/b3	0.0364	0.0395	0.0281	0.0031	0.0238	0.0027
d1/e2	0.0504	0.1080	0.1281	0.1188	0.1275	0.1182
f1/b4	0.0461	0.0257	0.0402	0.0090	0.0066	0.0063
b2/d5	0.0163	0.0416	0.0093	0.0006	0.0089	0.0006
e2/f5	0.0191	0.0562	0.0003	0.0013	0.0001	0.0001
d1/f5	0.0059	0.0086	0.0001	0.0003	0.0001	0.0000
d5/b4	0.0042	0.0038	0.0008	0.0006	0.0010	0.0005
f1/b6^S	0.0209	0.0493	0.0026	0.0294	0.0010	0.0034
f1/b6^R	0.0387	0.0780	0.0017	0.0928	0.0014	0.0076
f1/b5	0.0090	0.0087	0.0021	0.0157	0.0050	0.0837
e2/f1[g]	0.0000	0.0005	0.0269	0.0001	0.0040	0.0004
e2/b2[g]	0.0000	0.0010	0.0011	0.0160	0.0040	0.0265
e1/b4[g]	0.0000	0.0018	0.0017	0.0113	0.0018	0.0073
f1/b3[g]	0.0000	0.0017	0.0141	0.0026	0.0794	0.0972
R_d[h]		0.1008	0.2382	0.2467	0.3024	0.3538

NOE Data for Methyl Groups		distance (Å)				
cross-peak[d]	NOE$_{expt}$[e]	M1	M2	M3	M4	M5
d1/f6	0.0004	2.5	8.0	8.4	9.1	10.7
b2/d6	0.0027	2.3	2.3	5.0	2.3	5.2
e2/f6	0.0054	2.7	6.2	6.4	8.0	9.4
b4/d6	0.0017	2.8	4.2	5.2	3.9	5.2
b4/f6	0.0006	3.4	6.1	3.1	5.3	5.3

[a] Lower limit for experimental NOESY intensities is 0.0010. [b] For methyl protons, only distances are tabulated, in angstroms, instead of NOE intensities. [c] See Figure 1 for residue labels. [d] Only interresidue cross-peaks for the tetrasaccharide epitope are considered. [e] With an NOE mixing time (τ_m) of 40 ms. Intensities are normalized with V_0, the diagonal volume at zero mixing time. For methyl NOE connectivities, reported intensity is one-third of the cross-peak intensity. [f] Calculated with an effective rotation correlation time of 5.7 ns. [g] Negative NOE restraints, i.e., NOESY peaks not observed experimentally, yet used in NOESY intensity simulation to strengthen conformational analysis. [h] Negative peaks were not used for the calculation.

All the interresidue NOE connectivities observed at 40 ms mixing time are shown in Figure 3. NOE cross-peaks between anomeric and aglycon protons are all large, but unless a linkage shows an anti conformation, generally NOE cross-peaks across glycosidic linkages can be fitted to many different conformations. However, analyzing some of the other NOEs between adjacent as well as nonadjacent residues, makes it possible to identify a single conformation or to rule out the contribution of some others. Besides NOEs across glycosidic linkages between anomeric and aglyconic protons, there are many other long-range NOE connectivities such as **b** H2/**d** H5, **e** H2/**f** H5, **d** H1/**f** H5, and **d** H5/**b** H4, indicating the folded nature of the **d-e-b-f** tetrasaccharide fragment in the O139 polysaccharide. The lowest energy model, M1 gives the lowest R_d value (Table 4).

Although model M1 shows the best overall agreement with the experimental NOE data, some conformations such as M2 show a better fit for certain individual cross peaks such as that between **b** H2 and **d** H5 and between **f** H1 and H4. Therefore we have attempted to introduce minor populations of one or more of these conformations to a major population of M1 following a virtual conformation model (*28*). Although the R_d values are slightly reduced, the fitting of individual restraints does not become considerably better than for fitting M1 alone. Similarly, when the whole conformational cluster of family 1 was included for correlation between measured and calculated NOEs (*29*), no significant improvement over the fit of M1 itself was observed. The evidence from the 40 ms mixing time NOE data indicates that the primary conformation of the tetrasaccharide is M1.

Analysis of individual cross-peaks indicates why the virtual conformation model does not lead to major improvements in agreement with experiment and why M1 must represent the dominant conformer. The NOE cross-peak between **e** H2 and **f** H5 indicates that the lower surface of residue **f** is stacked over residue **e**. Similarly, the cross-peaks between **b** H2 and **d** H5 and between **b** H4 and **d** H5 indicates that colitose **d** is folded over GlcNAc **b**. But the pyranoside rings are slightly offset rather than directly stacked as is shown by the cross peaks between **f** H1 and **b** $H6^S$ and **b** $H6^R$, which show that **f** H1 is to be placed approximately between these two methylene protons as it is in model M1. Likewise, the cross-peak observed between **d** H1 and **f** H5 indicates the tight folding that brings the two colitose resides in proximity. Only the global minimum conformation M1 accounts for all these conformational features.

Addition of any significant population of conformations other than M1 to a virtual conformation model implies the appearance of some NOE cross-peaks that are not observed (Table 4). Model M2 implies a strong NOE between **e** H2 and **f** H1 rather than between **e** H2 and **f** H5 (see Figure 3 and Table 4). With GlcNAc (residue **b**) stacked above cyclic galactophosphate, conformation M3 would show a cross-peak between **e** H2 and **b** H2, rather than between **e** H2 and **f** H5; also, NOE across glycosidic linkage **e** H1/**b** H3 will be weaker than NOE to adjacent **e** H1/**b** H4, and **f** H1/**b** H5 will be stronger than **f** H1/**b** H4 (Table 4), contrary to the observed intensities. Similarly, the **f** H1/**b** H4 cross-peak across the glycosidic linkage between residues **f** and **b** would be weaker than **f** H1/**b** H3 with no possibility of an NOE between **e** H2 and **f** H5 if M4 were to have a significant population (Table 4). For conformational model M5, a strong **e** H2/**b** H2 signal should be obvious. M5 would show features of an anti conformation for the **f-b** glycosidic linkage, showing intense NOEs from **f** H1 to the two flanking protons **b** H3 and **b** H5 rather than with aglyconic **b** H4. A similar analysis carried out for the other conformations listed in Table 3 indicates that a significant population contribution to solution conformation from M2−M13 can be ruled out.

In addition to the interresidue NOE cross-peaks discussed so far, cross-peaks involving methyl groups of 6-deoxy sugars were observed experimentally (Figure 5 and Table 4.) Although they are not included in the calculation of simulated NOE because our treatment does not provide correct quantitative analysis of internal motion of methyl groups, qualitative analysis of these data supports the proposed model M1. When normalized to single proton values (Table 4), the methyl group NOE values are seen to be considerably smaller than those of the methine protons, presumably due to the difference in effective rotational correlation times. All distances to methyl groups listed for models in Table 4 refer to the distance to the most proximal proton. Folding of GlcNAc and colitose **d** can be seen in the strong NOE connectivity between 6-deoxy methyl of **d** and **b** H2 and **b** H4 (see Figure 5B,D). Similarly, folding of colitose **f** and galactose cyclic phosphate **e** is supported by the intense **e** H2/**f** H6 cross-peak in Figure 5C. Also, **f** H6 shows an NOE with **d** H1 (Figure 5A), providing further evidence for the turn of residue **f** we have proposed. While long-range methyl NOE cross-peaks we have discussed so far point to the highly folded model we propose for this tetrasaccharide fragment, there are also some short-range interresidue methyl NOE interactions such as that between **f** H6 and **b** H4 (Figure 5D) that support the conformation M1.

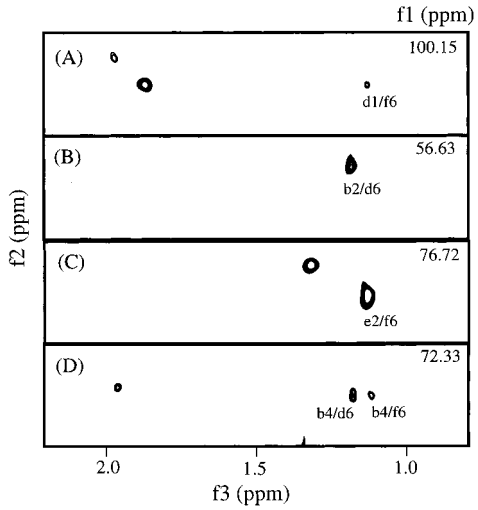

FIGURE 5: Two-dimensional NOESY strips from 3D HMQC-NOESY showing interresidue NOEs to methyl protons at a mixing time of 40 ms. ω_1 planes of donors are indicated on the right-hand side. Only cross peaks between **d-e-b-f** tetrasaccharide resonances are labeled. Labeling is simplified in that **d**1/**f**6 in strip A indicates the **d**H1/**f**H6 ($\omega_2-\omega_3$) cross-peak, etc.

On the basis of the increased number of NOE restraints from ^{13}C-edited NOESY we have reported above, together with our quantitative and qualitative analysis of data, we propose M1 as the major solution conformation of **d-e-b-f** tetrasaccharide fragment in the capsular polysaccharide of *V. cholerae*. It is a highly folded structure with the two colitoses extending above β-sides (*30*) of the core disaccharide β-D-gal(1 → 3)GlcNAcβ (*31*).

Although the NOESY cross-peaks in the spectrum taken at 100 ms mixing time are considerably stronger than those at 40 ms, all the peaks in the 40 ms are seen in the former. Some additional peaks observed are presumed to arise from the effects of spin diffusion at the longer mixing time. Although the spin simulation should in principle account for such effects, there are some assumptions in the simulation that may not be completely satisfied, leading to poor agreement. Thus the simulation of the NOE for the model M1 does not agree as well with experiment as the 40 ms data. Part of the discrepancy could arise from interactions with the protons of residues **a** and **c**, which are not included in the model.

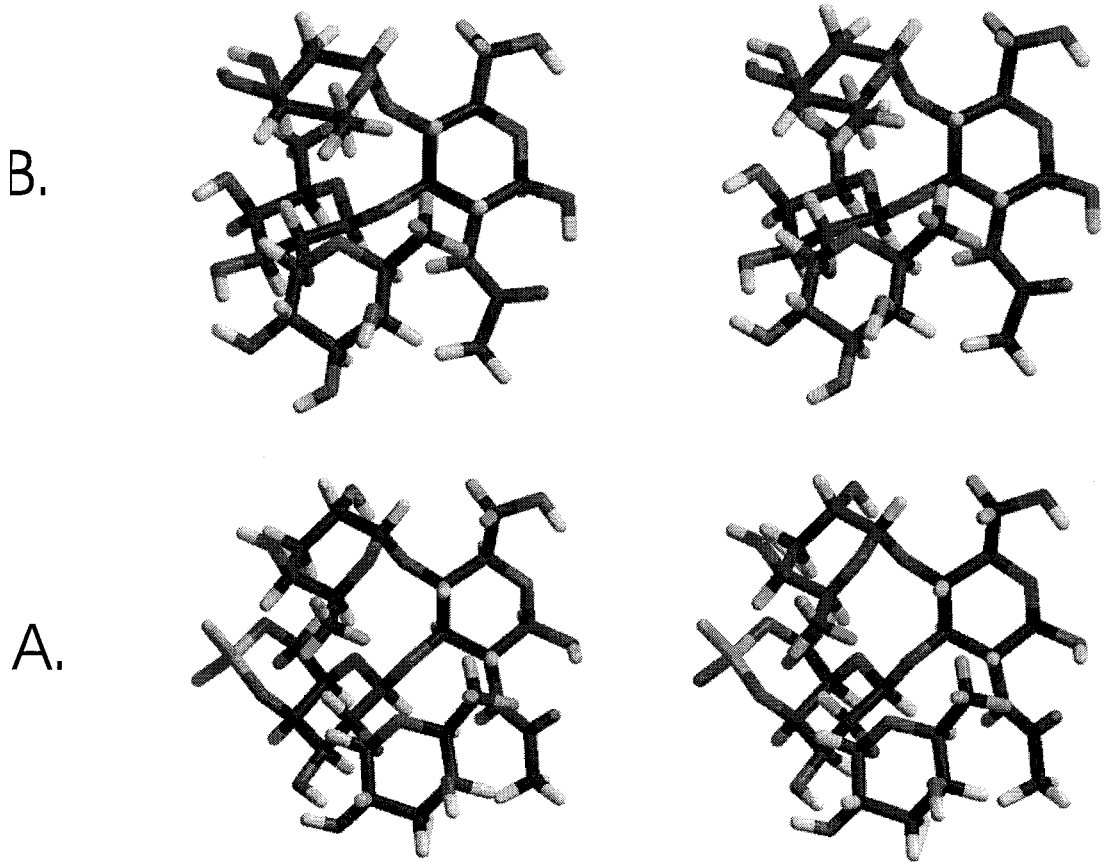

FIGURE 6: Stereopair models comparing M1 tetrasaccharide conformational model of O139 capsular polysaccharide (A, lower) and Le^b histo-blood group antigen (B, upper). Parameters are given in Table 3.

DISCUSSION

Figure 1 shows that there is a very close sequence homology between the **d**-**e**-**b**-**f** tetrasaccharide segment of *V. cholerae* capsular polysaccharide and the Le^b histo-blood group antigen tetrasaccharide epitope found in epithelial mucins and in the human milk oligosaccharide, lacto-*N*-difucohexaose 1 (LND1). The difference between the two tetrasaccharides is the replacement of the equatorial hydroxyl groups at C3 of the two residues of L-fucose by hydrogen atoms in the 3,6-dideoxy sugar L-colitose. The epitope of the O139 polysaccharide also includes the 4,6 cyclic phosphate on the β-galactose residue. Whether such a near sequence homology implies a similarity in three-dimensional conformation is a pertinent question that could have some implications to the mechanism of pathogenesis due to the mimicry of this common host epitope by the bacterium. Dot blot indirect ELISA assays also suggest some similarity of the CPS with the Le^b epitope. Mouse anti-Le^b (Immucor, Inc., Norcross, GA) gave moderately strong reactions (3+) with whole-cell AI1837 and purified CPS but not with whole cells or LPS from *V. cholerae* O1 (J. A. Johnson, unpublished data).

The conformation of the $Lewis^b$ tetrasaccharide has been previously studied by Lemieux et al. (*31*), who proposed a three-dimensional model on the basis of simple molecular modeling and qualitative NMR arguments. Subsequently, more extensive molecular modeling and quantitative NMR data have been used to confirm and revise the original model (*16*). X-ray crystallographic structure determination for the Le^b tetrasaccharide complexed with a lectin have also provided essentially the same conformation (*32*). Molecular dynamics simulations show that the conformational model is comparatively rigid and the root mean square fluctuations of the glycosidic dihedral angles are limited to approximately $\pm 10°$ (*33*). Extensive conformational mapping has shown that there is only a very small region of conformational space available to the $Lewis^b$ epitope. The convergence of these studies on a single consensus conformation for the Le^b epitope results from steric crowding, which leaves little conformational freedom for this particular stereochemical arrangement.

However, subtle differences between the two structures can be seen in analyzing the glycosidic torsion angles. The major difference is in the torsions for col-$\alpha(1 \rightarrow 2)$Gal linkage, where model M1 of the O139 polysaccharide (Table 3) shows a larger negative Φ_1 and a smaller positive Ψ_1 than does the model of Le^b. This is consistent with the observation of the cross-peak between **d** H1 and **f** H5 (Figure 3), which has not been reported for Le^b. The cross-peak between **d** H5 and **b** H4 (Figure 3) not seen in Le^b, supports the smaller negative Ψ_2 of M1. Similarly, the NOE cross-peak between **f** H1 and **b** H5 shown in Figure 3 supports the Φ_3 turn of col **f**. A comparison of the models for the Le^b tetrasaccharide and the tetrasaccharide epitope of the O139 polysaccharide is illustrated in Figure 6.

The differences in conformation between the O139 and the Le^b epitope presumably arise to accommodate the 4,6 cyclic phosphate group on the β-Gal residue of the O139 polysaccharide. A stereopair of the model of the O139 tetrasaccharide (Figure 6) shows that the col^2 **d** residue is

positioned relatively close to the GlcNAc residue in a conformation that is similar to the same residues in the Lewis^d epitope found in the milk oligosaccharide lacto-*N*-fucopentaose 1 (*34*, *35*, *29*). Likewise the α-col^4 residue **f** is positioned approximately parallel to and in close contact with the *β*-gal residue in a conformation similar to that of the Lewis^a epitope (*16*, *33*). The 4,6 cyclic phosphate on the *β*-galactose is accommodated in this conformation in close contact with the col^4 residue **f**. Knirel et al. (*8*) have observed consistent undermethylation of non-reducing-terminal colitose residues in structural studies of the capsular polysaccharide, an observation that could be explained by the crowding of the col^4 residue by the galactose phosphate. The model (Figure 6) shows that the cyclic phosphate is in close contact with the nonpolar face of col **f** with the proximal phosphate oxygen only 2.4 Å from **f** H4, a juxtaposition that might have some interesting electrostatic effect.

In principle, it should be possible with the ^{13}C-enriched polymer to measure ^{13}C scalar coupling constants to test the conformational model and give more insight into the nature of its flexibility. Preliminary $^3J_{CH}$ data are generally consistent with the proposed model but indicate that it may require some refinement. We suspect the detailed geometry of the cyclic phosphate, which has not been carefully parametrized, may not be completely correct in the model. Additional measurements, including ^{13}C−^{13}C coupling, may provide a definitive answer to this question.

The conformation of Le^b, in common with that of other blood group oligosaccharides, has been proposed to arise primarily from steric repulsion rather than from any specific interresidue hydrogen bonding or other polar interactions. The conformations of blood group oligosaccharides are stabilized by repulsive steric interactions, which are not disrupted by changes in temperature or of the solvent (*34*, *36*, *37*). It is most likely that it is the same steric interactions that are responsible for the tightly folded conformation observed for the tetrasaccharide epitope from the O139 polysaccharide.

While we are proposing a rigid tetrasaccharide epitope, we recognize that the capsular polysaccharide must also have elements of flexibility. A qualitative estimate of the dynamic character of the O139 polysaccharide identifies it as having intermediate flexibility. The NMR line widths and estimated effective rotational correlation times τ_c indicate that it is much less flexible than the cell wall polysaccharide of *Streptococcus mitis* J22, which contains a phosphodiester linkage, two 1 → 6 linkages, and a furanoside (*38*). But the O139 polysaccharide is more flexible than other capsular polysaccharides such as those previously studied in this laboratory from *Vibrio vulnificus* strains (*39*−*42*). These considerations imply that the O139 polysaccharide must have rather flexible hinges in the linkages that join the tetrasaccharide epitopes. The additional free rotation about the 1 → 6 linkage that joins *β*-QuiNAc and GlcNAc as well as the axial linkage between GlcNAc and C4 of GalA could contribute to the overall flexibility of the polysaccharide.

ACKNOWLEDGMENT

We thank Dr. Qiuwei Xu for helpful discussions about the NMR and molecular modeling techniques. We thank Dr. J. Glenn Morris, Jr., for continued encouragement on this project.

REFERENCES

1. Albert, M. J., Ansaruzzaman, M., Bardhan, P. K., Faruque, A. S. G., Islam, M. S., Mahalanabis, D., and Sack, R. B. (1993) *Lancet 342*, 387−390.
2. Waldor, M. K., Colwell, R., and Mekalanos, J. J. (1994) *Proc. Natl. Acad. Sci. 91*, 11388−11392.
3. Weintraub, A., Widmalm, G., Jansson, P. E., Jansson, M., Hultenby, K., and Albert, M. J. (1994) *Microb. Pathogen. 16*, 235−241.
4. Johnson, J. A., Salles, C. A., Panigrahi, P., Albert, M. J., Wright, A. C., Johnson, R. J., and Morris, J. G., Jr. (1994) *Infect. Immun. 62*, 2108−2110.
5. Comstock, L. E., Maneval, D., Panigrahi, P., Joseph, A., Levine, M. M., Kaper, J. B., Morris, J. G., and Johnson, J. A. (1995) *Infect. Immun. 63*, 317−323.
6. Mitra, R., Basu, A., Dutta, D., Nair, G. B., and Takeda, Y. (1996) *Lancet 348*, 1181.
7. Preston, L. M., Xu, Q., Johnson, J. A., Joseph, A., Maneval, D. R., Husain, K., Reddy, G. P., Bush, C. A., and Morris, J. G. (1995) *J. Bacteriol. 177*, 835−838.
8. Knirel, Y. A., Paredes, L., Jansson, P. E., Weintraub, A., Widmalm, G., and Albert, M. J. (1995) *Eur. J. Biochem. 232*, 391−396.
9. Cox, A. D., and Perry, M. B. (1996) *Carbohydr. Res. 290*, 59−65.
10. Johnson, J. A., Joseph, A., and Morris, J. G., Jr. (1995) *Inst. Pasteur (Paris) 93*, 285−290.
11. Morris, J. G., Jr., Losonsky, G. E., Johnson, J. A., Tacket, C. O., Nataro, J. P., Panigrahi, P., and Levin, M. M. (1995) *J. Infect. Dis. 171*, 903−908.
12. Johnson, J. A., Panigrahi, P., and Morris, J. G. (1992) *Infect. Immun. 60*, 864−869.
13. Fesik, S. W., and Zuiderweg, E. R. P. (1988) *J. Magn. Reson. 78*, 588−593.
14. Ha, S. N., Giammona, A., Field, M., and Brady, J. W. (1988) *Carbohydr. Res. 180*, 207−221.
15. Keepers, J. W., and James, T. L. (1984) *J. Magn. Reson. 57*, 404−426.
16. Cagas, P., and Bush, A. (1990) *Biopolymers 30*, 1123−1138.
17. Bush, C. A. (1994) *Methods Enzymol. 240*, 446−459.
18. Xu, Q., Mohan, S., and Bush, A. (1996) *Biopolymers 38*, 339−353.
19. Shriver, J., and Edmonson, S. (1993) *Biochemistry 32*, 1610−1617.
20. Podlasek, C. A., Wu, J., Stripe, W. A., Bondo, P. B., and Serianni, A. S. (1995) *J. Am. Chem. Soc. 117*, 8635−8644.
21. Bundle, D. R., Eichler, E., Gidney, M. A. J., Meldal, M., Ragauskas, A., Sigurskjold, B. W., Sinnott, B., Watson, D. C., Yaguchi, M., and Young, N. M. (1994) *Biochemistry 33*, 5172−5182.
22. Hall, L. D., and Malcolm, R. B. (1972) *Can. J. Chem. 50*, 2092−2101.
23. Jones, D. N. M., and Sanders, J. K. M. (1989) *J. Am. Chem. Soc. 111*, 5132−5137.
24. Beale, J. M., and Foster, J. L. (1996) *Biochemistry 35*, 4492−4501.
25. Sheng, S., and Cherniak, R. (1997) *Carbohydr. Res. 301*, 33−40.
26. Kjellberg, A., Nishida, T., Weintraub, A., and Widmalm, G. (1998) *Magn. Res. Chem. 35*, 128−131.
27. Gitti, R., Long, G., and Bush. C. A. (1994) *Biopolymers 34*, 1327−1338.
28. Cumming, D. A., and Carver, J. P. (1987) *Biochemistry 26*, 6664−6676.
29. Duus, J. O., Nifant'ev, N., Shashkov, A. S., Khatuntseva, E. A., and Bock, K. (1996) *Carbohydr. Res. 288*, 25−44.
30. Stoddart, J. F. (1971) *Stereochemistry of Carbohydrates*, p 32, Wiley-Interscience, New York.
31. Lemieux, R. U., Bock, K., Delbaere, L. T. J., Koto, S., and Rao, V. S. (1980) *Can. J. Chem. 58*, 631−653.

32. Delbaere, L. T., Vandonselaar, M., and Prasad, L. (1993) *J. Mol. Biol. 230*, 950−965.
33. Mukhopadhyay, C., and Bush, A. (1991) *Biopolymers 31*, 1737−1746.
34. Rao, B. N. N., Dua, V. K., and Bush, A. (1985) *Biopolymers 24*, 2207−2229.
35. Yan, Z. Y., and Bush, A. (1990) *Biopolymers 29*, 799−811.
36. Bush, C. A., Yan, Z. Y., and Rao, B. N. N. (1986) *J. Am. Chem. Soc. 108*, 6168−6173.
37. Yan, Z. Y., Rao, B. N. N., and Bush, C. A. (1987) *J. Am. Chem. Soc. 109*, 7663−7669.
38. Xu, Q., and Bush, C. A. (1996) *Biochemistry 35*, 14521−14529.
39. Reddy, G. P., Hayat, U., Abeygunawardana, C., Fox, C., Wright, A. C., Maneval, D. R., Bush, C. A., and Morris, J. G. (1992) *J. Bacteriol. 174*, 2620−2630.
40. Reddy, G. P., Hayat, U., Bush, C. A., and Morris, J. G. (1993) *Anal. Biochem. 21*, 106−115.
41. Reddy, G. P., Hayat, U., Xu, Q., Reddy, K. V., Wang, Y., Chiu, K. W., Morris, J. G., and Bush, C. A. (1998) *Eur. J. Biochem. 255*, 279−288.
42. Gunawardena, S., Reddy, G. P., Wang, Y., Kumar Kolli, V. S., Orlando, R., Morris, J. G., and Bush, C. A. (1998) *Carbohydr. Res. 309*, 65−76.

BI9910272